COMMUNICATION

Check for updates

Self-assembled metal–organic framework composed of one-dimensional Rh(II/III) chains with an octahedral [RhN$_6$] coordination†

Ai Kurahashi, Yukihiro Yoshida [ID] * and Hiroshi Kitagawa [ID] *

A mixed-valence rhodium(II/III)-based metal–organic framework with an octahedral [RhN$_6$] coordination was synthesised for the first time in this study. The porous structure leads to a considerable amount of N$_2$, H$_2$, and CO$_2$ gas adsorption and a relatively high proton conductivity when water molecules are adsorbed in the channel pores.

Over the past two decades, metal–organic frameworks (MOFs) have been a subject of intense research as a new class of porous materials aimed at practical applications such as gas storage/separation, catalysis, and electrochemical energy storage.[1–3] A central driving force behind research into MOFs is the benefit of the control of chemical and physical properties, such as porous and pore surface structures, by judicious design or choice of the component metal nodes (ions or clusters) and multitopic organic linkers. In this regard, it is essential to explore a metal–ligand combination that has not been exploited previously, in order to expand the research territory in the field of functional MOFs. To this end, in this study, we focused on Rh-based MOFs, because the Rh-based cluster in MOFs has been limited to a paddlewheel-type dinuclear unit, [Rh$_2$(O$_2$CR)$_4$] (Fig. 1a),[4–7] which has provided various aggregation structures, including dimers,[8] triangles,[9] polyhedra,[10] one-dimensional (1D) linear chains,[11–15] two-dimensional (2D) sheets,[16,17] and three-dimensional (3D) diamond lattice.[18] Therefore, the exploration of new members of metal–ligand combination in Rh-based MOFs inevitably opens up opportunities for the rational control of the chemical and physical properties of the Rh-based MOFs.

In this study, we successfully synthesised a Rh-based MOF, Rh$_2$(H$_x$bdtz)$_3$·nH$_2$O (H$_2$bdtz: 5,5′-(1,4-phenylene)bis(1*H*-tetrazole), see Fig. 1b; $n \sim 19$); octahedrally coordinated Rh(II/III) ions are bridged by three μ^2-tetrazolate moieties of bdtz^{2-} ligands (Fig. 1a) to form the 1D chains, which are connected by the bis-bidentate bdtz^{2-} ligands to form the 3D porous structure. To the best of our knowledge, this is the first example of a MOF with Rh ions in an octahedral [RhN$_6$] coordination environment. In addition, there is yet to be a synthesis of the MOF with mixed-valence Rh(II/III) ions. To characterise the porous properties, the adsorption isotherms of several gases (N$_2$, H$_2$, and CO$_2$) and proton conduction under conditions in which water molecules were adsorbed in the channel pores were investigated.

A solvothermal reaction of RhCl$_3$·3H$_2$O, H$_2$bdtz, and K$_2$CO$_3$ in water/ethanol (3 : 7) mixed solvent at 80 °C produced brown polycrystalline solids (see ESI,† for synthetic details; Fig. S1 in ESI†). As shown in Fig. 1c, the powder X-ray diffraction (PXRD) pattern of the product exhibits several broad peaks centred at $2\theta \sim 7.6$, 15.0, and 27.5°. This reminds us of 3D MOFs, M$_2$(H$_x$bdtz)$_3$·nH$_2$O (n = 13 or 17 for Fe,[19–22] n = 20 for Co,[23] and n = 10.5 for Ni[24]) (Fig. S2 in ESI†), in which 1D chains composed of octahedrally coordinated metal ions are linked with each other by bis-bidentate bdtz^{2-} ligands. The scanning electron microscope (SEM) image of the product shows the undefined morphology (Fig. 2a). The Rh–N coordination of the bdtz^{2-} ligands was verified by the almost disappearance of the N–H stretching band (3366 cm^{-1}) in the Fourier transform infrared (FTIR) spectrum (Fig. S3 in ESI†). In addition, the Fourier transformed extended X-ray absorption fine structure (EXAFS) spectrum at the Rh K-edge of the product (Fig. S4 in ESI†) shows only a first-shell peak at 2.07 Å (Fig. 2b), which is assigned to the Rh–N bond.[25] The estimated coordination number of 6.4(4) is in good agreement with that expected from the proposed structure (Fig. 1d and e). As shown in Fig. 2c, the X-ray absorption near-edge structure (XANES) of the product shows a threshold value of 23 223.6 eV, which lies between those of Rh^{II}(OAc)$_2$ (23 220.9 eV) and Rh^{III}(acac)$_3$ (23 224.1 eV; Hacac: acetylacetone), indicating a mixed-valence Rh(II/III) state. It is possible that ethanol in the reaction mixture causes the

Division of Chemistry, Graduate School of Science, Kyoto University, Kitashirakawa-Oiwakecho, Sakyo-ku, Kyoto 606-8502, Japan
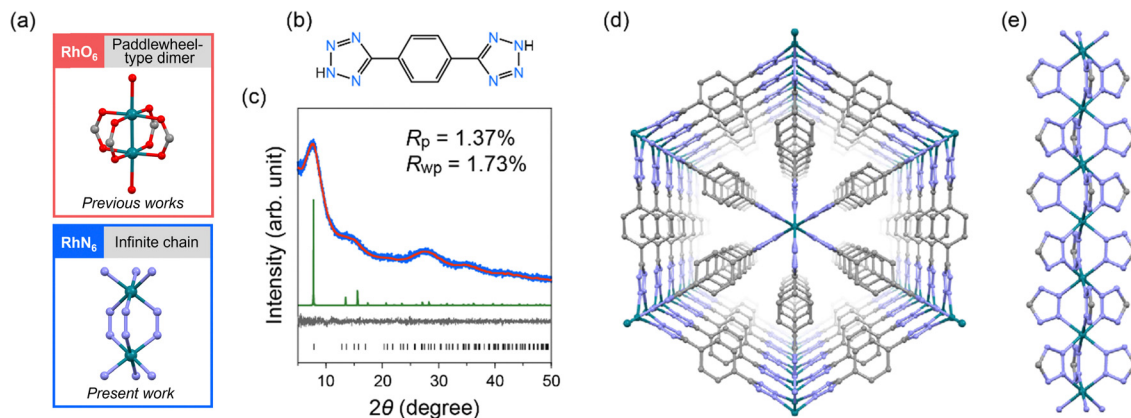*E-mail: yoshiday@ssc.kuchem.kyoto-u.ac.jp, kitagawa@kuchem.kyoto-u.ac.jp*

Fig. 1 (a) Coordination environments of (top) [Rh$_2$(O$_2$CR)$_4$] (apical oxygen atoms are attributed to coordinated solvent molecules) and (bottom) [RhN$_6$] in **1**. (b) Molecular structure of H$_2$bdtz. (c) Experimental PXRD pattern (blue), Pawley-refined fitting (red), their difference (grey), and calculated pattern from structural model (green). Simulated structures viewed along (d) the *c* axis and (e) the *a* axis. Colour code: C: grey; N: purple; O: red; Rh: green.

partial reduction of Rh(III) ions in the starting material, RhCl$_3$·3H$_2$O.[26] Because it became evident that the product was isostructural with M$_2$(H$_x$bdtz)$_3$·nH$_2$O (M = Fe, Co, and Ni), the crystal structure was simulated based on the PXRD pattern with a trigonal lattice with space group $R\bar{3}m$ (Fig. 1d, e, and Fig. S5 in ESI†).[20,21] The lattice parameters were estimated to be a = 22.705 Å and c = 6.972 Å using the Pawley refinement. These values are slightly smaller than the corresponding values in Fe$_2$(H$_x$bdtz)$_3$·13H$_2$O (a = 22.604(4) Å and c = 7.454(3) Å),[19] which are a reflection of the difference in ion radius between Rh(III) ion (0.665 Å) and high-spin Fe(II) ion (0.780 Å).[27] Elemental analysis confirmed the composition, Rh$_2$(H$_x$bdtz)$_3$·nH$_2$O (hereafter abbreviated as **1**), when the n value is equal to be approximately 19 (ESI†). Water vapour sorption measurements confirmed that the dehydrated **1** is capable of absorbing the large amount of water (approximately 22 wt%) at 95% RH (relative humidity; Fig. 2d). The amount of the adsorbed water molecules (approximately 11 water molecules per formula unit) is lower than the composition estimated from the elemental analysis (approximately 19 water molecules per formula unit). This discrepancy may indicate that a considerable amount of water molecules is physically attached onto the surface of the particles under ambient conditions. Grand canonical Monte Carlo simulations suggested that there are several C–H⋯O hydrogen bonding interactions with an H⋯O distance of 2.88–2.95 Å (*vs.* van der Waals radii: 2.72 Å)[28] and π⋯O interactions with a C⋯O distance of 3.48 Å (*vs.* van der Waals radii: 3.32 Å)[28,29] between the ligands and adsorbed H$_2$O molecules. Thermogravimetric and PXRD studies revealed that compound **1** is thermally stable up to approximately 300 °C (Fig. S7 and S8 in ESI†). We note that compound **1** showed high tolerance to typical solvents such as water (ε_r = 78.3), ethanol (ε_r = 24.6), acetone (ε_r = 20.7), and diethyl ether (ε_r = 4.2) (Fig. S9 in ESI†), where ε_r is the relative permittivity.

X-ray photoelectron spectroscopy (XPS) measurements of **1** were performed to further elucidate the valence states of the Rh ions (Fig. 2e). The peaks observed at approximately 317 eV and 312 eV were assigned to Rh 3d$_{3/2}$ and Rh 3d$_{5/2}$, respectively.
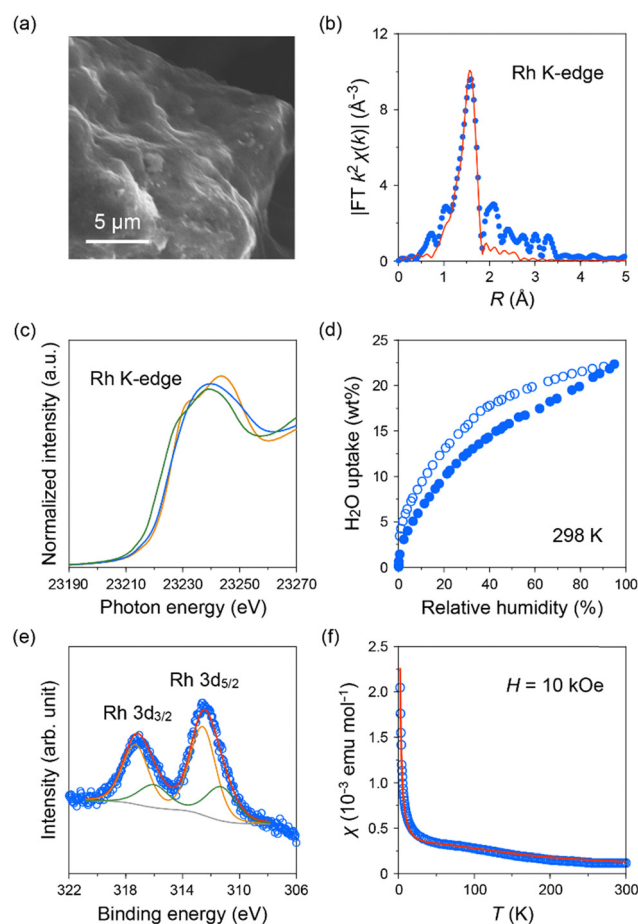

Fig. 2 (a) SEM image, (b) Fourier transformed EXAFS spectrum at the Rh K-edge (blue circles: measured spectrum, red line: fitting curve, χ: EXAFS oscillation), (c) Rh K-edge XANES spectra (**1**: blue, Rh(OAc)$_2$: green, Rh(acac)$_3$: orange), (d) H$_2$O vapour adsorption (closed circles) and desorption (open circles) isotherms at 298 K, (e) Rh-3d XPS (blue open circles: measured spectrum, red line: fitting curve, orange and green curves: components of the fitting curve, grey: background), and (f) temperature dependence of magnetic susceptibility (χ) under H = 10 kOe (see text for a red line).

We note that both peaks consist primarily of two components, 317.3 and 316.1 eV for the former and 312.6 and 311.4 eV for the latter. The splitting of *ca.* 1 eV observed for each peak strongly indicates mixed-valence Rh(II/III) ions[30,31] as expected from the XANES spectrum. Regardless of the Rh(II)/Rh(III) ratio, the inclusion of Rh(II) ions requires the protons (x) on the bdtz^{2-} ligands to compensate the charge in the solid (*i.e.*, $x = 0.67$ for only Rh(II) and $x = 0$ for only Rh(III)), as argued in $M_2(H_x$bdtz$)_3 \cdot nH_2O$ (M = Fe, Co, and Ni)[19–24]. Magnetic susceptibility (χ) measurement was conducted in an applied magnetic field of 10 kOe to confirm the presence of d^7 Rh(II) ions in **1**, because octahedrally coordinated d^6 Rh(III) ions are generally in low spin state with fully occupied t_{2g} and empty e_g sets. The χ value was estimated to be 1.2×10^{-4} emu mol^{-1} at 300 K, and increases with decreasing temperature as shown in Fig. 2f. The temperature dependence can be described by the Heisenberg antiferromagnetic chain model[32] with $J/k_B = -47$ K (k_B: Boltzmann constant) of *ca.* 6.0% of $S = 1/2$ spins on Rh(II) ions. Given that the neighbouring Rh···Rh distance is rather long (*ca.* 3.71 Å), the antiferromagnetic interaction is predominantly driven from the superexchange pathways through nitrogen atoms in bridging bdtz^{2-} ligands. The upturn of χ at low temperatures ($T < ca.$ 20 K) arises from *ca.* 1.5% of Curie-like paramagnetic spins such as Rh(II) ion isolated by diamagnetic Rh(III) ions as well as defects and impurity. The magnetic susceptibility data possibly indicate the formation of an inhomogeneous valence arrangement with a Rh(II)/Rh(III) ratio of *ca.* 0.08 [= (6.0 + 1.5)/92.5] in the 1D chain (Fig. S10 in ESI†). It is likely that the low Rh(II)/Rh(III) ratio is consistent with XANES (Fig. 2c) and XPS (Fig. 2e) results. Notably, the spin state of Rh(III) ions is consistent with those of a low spin state of isostructural MOF, Fe$_2$(H$_x$bdtz)$_3 \cdot 13$H$_2$O, that undergoes a spin crossover.[19,20] The possible valence inhomogeneity is consistent with the high DC resistivity that exceeds the measurement limit ($> 5 \times 10^8$ Ω cm).

To verify the porous structure as in M$_2$(H$_x$bdtz)$_3 \cdot n$H$_2$O (M = Fe,[19–22] Co,[23] and Ni[24]), the N$_2$ gas sorption isotherm of **1** was measured at 77 K (Fig. 3a), in which there is a pronounced uptake at $P/P_0 < 0.02$ as manifestation of the presence of micropores with MOF-type structure. The average pore size (0.73 nm) estimated using the grand canonical Monte Carlo (GCMC) simulation (Fig. 3b) was comparable to that expected from the simulated crystal structure (*ca.* 0.75 nm).
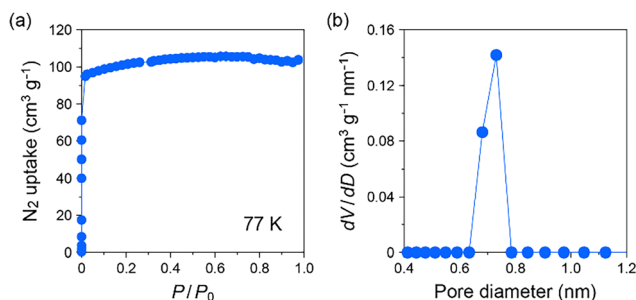
The Brunauer–Emmett–Teller (BET) surface area was estimated to be 386 m^2 g^{-1}, which is lower than that reported for isomorphous Fe (614 m^2 g^{-1}; ref. 21) and Co (729 m^2 g^{-1}; ref. 23) MOFs, possibly due to the poor crystallinity. In addition, compound **1** exhibited a pronounced adsorption capacity for H$_2$ (37.5 cm^3 g^{-1}, 1.67 mmol g^{-1}, and 0.34 wt% at 77 K) and CO$_2$ (90.4 cm^3 g^{-1}, 4.04 mmol g^{-1}, and 17.8 wt% at 195 K) as shown in Fig. S11 and S12, respectively, in ESI.†

The presence of acidic protons (x) in the bdtz^{2-} ligands promoted us to examine the proton-conducting behaviour of **1**, because one of the most characteristic properties of acidic MOFs is their significant proton conductivity.[33–35] We measured the AC impedance spectra of the compressed pellet of **1** (2.5 mm in diameter) with an applied voltage of 100 mV under various conditions. Fig. 4a displays the RH dependence of the Nyquist plot of the impedance data at 298 K, where the proton conductivity (σ) was estimated by fitting the plot with an appropriate equivalent circuit shown in Fig. S13 in ESI.† As shown in Fig. 4b, the σ value steadily increases as RH increases, and eventually reaches 7.0×10^{-5} S cm^{-1} under 98% RH. Considering that the water vapour sorption isotherm exhibits a continuous increase in water uptake up to 95% RH (Fig. 2d), the RH dependence must reflect the concentration of water in the pores, which can serve as Lewis basic sites for proton hopping. To the best of our knowledge, there have been no reports on proton conducting behavior of tetrazolate-bridged MOFs. Notably, pyrazolate-bridged Ni-based MOFs exhibited a proton conductivity on the order of 10^{-5} to 10^{-6} S cm^{-1} at 25 °C under 97% RH,[36] which is comparable to that of the present MOF. The water density in the pores (1.01 g cm^{-3}) is

Fig. 3 (a) N$_2$ gas adsorption isotherm at 77 K and (b) pore size distribution estimated using the GCMC method.
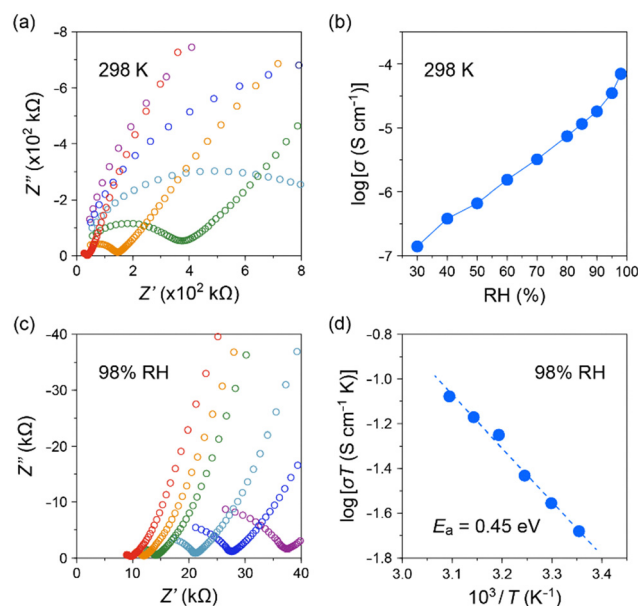

Fig. 4 (a) Nyquist plots (purple: 50% RH, blue: 60% RH, pale blue: 70% RH, green: 80% RH, orange: 90% RH, red: 98% RH) and (b) proton conductivity (σ) at 25 °C under various RHs and (c) Nyquist plots (purple: 25 °C, blue: 30 °C, pale blue: 35 °C, green: 40 °C, orange: 45 °C, red: 50 °C) and (d) σ at various temperatures under 98% RH. In (d), the dotted line is fit to the Arrhenius equation.

comparable to that of bulk water, thereby indicating the formation of efficient proton-conducting pathway *via* water···-water O–H···O hydrogen bonds. In the pathway, the acidic proton attached to the ligands can act as a proton source. The σ value exhibits a thermal activation (298–323 K; Fig. 4c and d) under 98% RH and the highest value is 2.6×10^{-4} S cm^{-1} at 323 K. The activation energy (E_a) was estimated to be 0.45 eV using the Arrhenius equation given by $\sigma T = A \exp(-E_a/k_B T)$ (A: pre-exponential factor). The relatively low E_a value suggests that proton migration is primarily governed by the Grotthuss mechanism,[37,38] which refers to proton mediation by infinite hydrogen bonding networks formed by protonated H$_x$bdtz$^{(2-x)-}$ ligands and guest water molecules. The PXRD study revealed that the structure of **1** was mostly intact during the impedance measurements (Fig. S14 in ESI†).

In summary, we successfully synthesised the first MOF constructed using 1D Rh(II/III) chains bridged by bis-bidentate bdtz^{2-} ligands, which is strikingly different from the reported Rh-based MOFs based on paddlewheel-type Rh$_2$(O$_2$CR)$_4$ cluster units. The structure and composition of the MOF were characterised by X-ray diffraction, elemental analysis, and optical approaches. The microporous structure facilitates the adsorption of a considerable amount of various gases. The presence of acidic proton attached to the ligands, which is required for having the mixed-valence Rh(II/III) state, can result in relatively high proton conductivity when water molecules are adsorbed in the micropores. The present results provide an initial step toward the future exploration of Rh-based MOFs through the rational selection of ligand species.

Data availability

The data supporting this article have been included as part of the ESI.†

Conflicts of interest

There are no conflicts to declare.

Notes and references

1 A. Schoedel, M. Li, D. Li, M. O'Keeffe and O. Yaghi, *Chem. Rev.*, 2016, **116**, 12466–12535.
2 A. Dhakshinamoorthy, Z. Li and H. Garcia, *Chem. Soc. Rev.*, 2018, **47**, 8134–8172.
3 N. Behera, J. Duan, W. Jin and S. Kitagawa, *EnergyChem*, 2021, **3**, 100067.
4 T. Sato, W. Mori, C. Nozaki Kato, E. Yanaoka, T. Kuribayashi, R. Ohtera and Y. Shiraishi, *J. Catal.*, 2005, **232**, 186–198.
5 L. Chen, T. Yang, H. Cui, T. Cai, L. Zhang and C.-Y. Su, *J. Mater. Chem. A*, 2015, **3**, 20201–20209.
6 T. Grancha, A. Carné-Sánchez, F. Zarekarizi, L. Hernández-López, J. Albalad, A. Khobotov, V. Guillerm, A. Morsali, J. Juanhuix, F. Gándara, I. Imaz and D. Maspoch, *Angew. Chem., Int. Ed.*, 2021, **60**, 5729–5733.
7 A. C. Ghosh, A. Legrand, R. Rajapaksha, G. A. Craig, C. Sassoye, G. Balázs, D. Farrusseng, S. Furukawa, J. Canivet and F. M. Wisser, *J. Am. Chem. Soc.*, 2022, **144**, 3626–3636.
8 Y. Kataoka, K. Arakawa, H. Ueda, N. Yano, T. Kawamoto and M. Handa, *Dalton Trans.*, 2018, **47**, 17233–17242.
9 F. A. Cotton, C. A. Murillo, S.-E. Stiriba, X. Wang and R. Yu, *Inorg. Chem.*, 2005, **44**, 8223–8233.
10 J. Troyano, S. Horike and S. Furukawa, *J. Am. Chem. Soc.*, 2022, **144**, 19475–19484.
11 Z. Yang, T. Fujinami, M. Ebihara, K. Nakajima, H. Kitagawa and T. Kawamura, *Chem. Lett.*, 2000, 1006–1007.
12 Z. Yang, M. Ebihara, T. Kawamura, T. Okubo and T. Mitani, *Inorg. Chim. Acta*, 2001, **321**, 97–106.
13 M. Ebihara and Y. Fuma, *Acta Crystallogr.*, 2006, **C62**, m556–m558.
14 Z. Yang, M. Ebihara and T. Kawamura, *Inorg. Chim. Acta*, 2006, **359**, 2465–2471.
15 P. Amo-Ochoa, R. Jiménez-Aparicio, M. R. Torres, F. A. Urbanos, A. Gallego and C. J. Gómez-García, *Eur. J. Inorg. Chem.*, 2010, 4924–4932.
16 Y. Takazaki, Z. Yang, M. Ebihara, K. Inoue and T. Kawamura, *Chem. Lett.*, 2003, **32**, 120–121.
17 Y. Fuma and M. Ebihara, *Chem. Lett.*, 2006, **35**, 1298–1299.
18 Y. Fuma, M. Ebihara, S. Kutsumizu and T. Kawamura, *J. Am. Chem. Soc.*, 2004, **126**, 12238–12239.
19 Z. Yan, M. Li, H.-L. Gao, X.-C. Huang and D. Li, *Chem. Commun.*, 2012, **48**, 3960–3962.
20 W.-T. Liu, J.-Y. Li, Z.-P. Ni, X. Bao, Y.-C. Ou, J.-D. Leng, J.-L. Liu and M.-L. Tong, *Cryst. Growth Des.*, 2012, **12**, 1482–1488.
21 L. S. Xie, L. Sun, R. Wan, S. S. Park, J. A. DeGayner, C. H. Hendon and M. Dincă, *J. Am. Chem. Soc.*, 2018, **140**, 7411–7414.
22 A. Martinez-Martinez, E. Resines-Urien, L. Piñeiro-López, A. Fernández-Blanco, A. L. Mariano, J. Albalad, D. Maspoch, R. Poloni, J. A. Rodríguez-Velamazán, E. C. Sañudo and E. Burzurí, *Chem. Mater.*, 2023, **35**, 6012–6023.
23 W. Ouellette, A. V. Prosvirin, K. Whitenack, K. R. Dunbar and J. Zubieta, *Angew. Chem., Int. Ed.*, 2009, **48**, 2140–2143.
24 W. Ouellette, K. Darling, A. Prosvirin, K. Whitenack, K. R. Dunbar and J. Zubieta, *Dalton Trans.*, 2011, **40**, 12288–12300.
25 C. E. Housecroft, *Coord. Chem. Rev.*, 1992, **115**, 191–230.
26 N. Toshima and T. Yonezawa, *New J. Chem.*, 1998, **22**, 1179–1201.
27 R. D. Shannon, *Acta Crystallogr.*, 1976, **A32**, 751–767.
28 A. Bondi, *J. Phys. Chem.*, 1964, **68**, 441–451.
29 D. P. Malenov, G. V. Janjić, D. Ž. Veljković and S. D. Zarić, *Comput. Theor. Chem.*, 2013, **1018**, 59–65.
30 C. Furlani, G. Mattogno, G. Polzonetti, G. Sbrana and G. Valentini, *J. Catal.*, 1985, **94**, 335–342.
31 J. Wolf, R. Poli, J.-H. Xie, J. Nichols, B. Xi, P. Zavalij and M. P. Doyle, *Organometallics*, 2008, **27**, 5836–5845.
32 J. C. Bonner and M. E. Fisher, *Phys. Rev.*, 1964, **135**, A640–A658.
33 P. Ramaswamy, N. E. Wong and G. K. H. Shimizu, *Chem. Soc. Rev.*, 2014, **43**, 5913–5932.
34 Y. Ye, L. Gong, S. Xiang, Z. Zhang and B. Chen, *Adv. Mater.*, 2020, **32**, 1907090.
35 D.-W. Lim and H. Kitagawa, *Chem. Rev.*, 2020, **120**, 8416–8467.
36 T. He, Y.-Z. Zhang, H. Wu, X.-J. Kong, X.-M. Liu, L.-H. Xie, Y. Dou and J.-R. Li, *Chem. Phys. Chem.*, 2017, **18**, 3245–3252.
37 N. Agmon, *Chem. Phys. Lett.*, 1995, **244**, 456–462.
38 K.-D. Kreuer, *Chem. Mater.*, 1996, **8**, 610–641.